

Pushing the boundaries
of chemistry?
It takes
#HumanChemistry

Make your curiosity and talent as a chemist matter to the world with a specialty chemicals leader. Together, we combine cutting-edge science with engineering expertise to create solutions that answer real-world problems. Find out how our approach to technology creates more opportunities for growth, and see what chemistry can do for you at:

[evonik.com/career](https://www.evonik.com/career)



Selective Vertical and Horizontal Growth of 2D WS₂ Revealed by In Situ Thermolysis using Transmission Electron Microscopy

Dnyaneshwar S. Gavhane,* Atul D. Sontakke, and Marijn A. van Huis*

Direct observation of the growth dynamics of 2D transition metal dichalcogenides (TMDs) is of key importance for understanding and controlling the growth modes and for tailoring these intriguing materials to desired orientations and layer thicknesses. Here, various stages and multiple growth modes in the formation of WS₂ layers on different substrates through thermolysis of a single solid-state (NH₄)₂WS₄ precursor are revealed using in situ transmission electron microscopy. Control over vertical and horizontal growth is achieved by varying the thickness of the drop-casted precursor from which WS₂ is grown during heating. First depositing platinum (Pt) and gold (Au) on the heating chips much enhance the growth process of WS₂ resulting in an increased length of vertical layers and in a self-limited thickness of horizontal layers. Interference patterns are formed by the mutual rotation of two WS₂ layers by various angles on metal deposited heating chips. This shows detailed insights into the growth dynamics of 2D WS₂ as a function of temperature, thereby establishing control over orientation and size. These findings also unveil the important role of metal substrates in the evolution of WS₂ structures, offering general and effective pathways for nano-engineering of 2D TMDs for a variety of applications.

yield comparable to MoS₂ implies promising candidature of monolayer WS₂ in 2D optoelectronic devices.^[3,8,9] Considering its exceptional electronic properties, efforts were made to use single layer and multilayer WS₂ as a thin film transistor.^[4,10] Various synthesis routes were employed to prepare thin WS₂ layers ranging from single to few layers.^[11–13] Through the conventional chemical routes, like chemical vapor deposition (CVD), horizontally grown WS₂ layers on the substrate with basal plane orientation exposing terrace sites, can be prepared with a large area.^[14–17] WS₂ layers can be grown with a vertical orientation, standing upright on the substrate exposing the edge sites.^[18] Horizontal WS₂ layers can be used in optoelectronics and electronics,^[10,19–21] and vertically aligned WS₂ layers are used as catalysts for the hydrogen evolution reaction (HER) due to their chemically reactive edge sites.^[22,23] Thus, depending

1. Introduction

2D layered WS₂, an important member of the transition metal dichalcogenides (TMDs) family having a direct bandgap, displays intriguing physical and chemical properties and is used for a multitude of applications in electronics and optoelectronics.^[1–7] High photoluminescence quantum


on the orientation of the 2D layers on the growth substrate, WS₂ exhibits distinctive properties suited for specific applications.

Thermal decomposition of ammonium tetra-thio tungstate (ATT), an amorphous single solid-state precursor, produces WS₂ structures.^[24,25] Synthesis of WS₂ from this single precursor is straightforward and no specific conditions are required to decompose it thermally. Few efforts were made to use this unique synthesis method to produce WS₂ structures.^[26,27] Apart from those studies, this synthesis route has not been explored much in comparison to other more conventional synthesis methods. An amorphous and single solid-state precursor provides an exceptional opportunity to grow and explore the underlying growth mechanisms of WS₂ structures.

The conventional CVD method is the most commonly used technique to grow large area, pure, and monolayer thin 2D TMDs, including WS₂ layers grown on a SiO₂/Si substrate.^[11,16–18,28,29] Growth of WS₂ on the amorphous and inert SiO₂/Si substrate usually forms randomly oriented domains with high angle grain boundaries,^[14] having low quality and uncontrolled structure.^[11–13,16,30] Also, in order to transfer WS₂ materials grown via CVD from an inert substrate, it has to go through a substrate etching process by using acidic or basic solutions.^[11,13,16,30] This causes unwanted damage to the WS₂ material and substrate residues contaminate the material to some extent.^[31] A single crystal c-plane (0001) sapphire wafer

D. S. Gavhane, M. A. van Huis
Soft Condensed Matter
Debye Institute for Nanomaterials Science
Utrecht University
Princetonplein 5, Utrecht 3584 CC, The Netherlands
E-mail: d.s.gavhane@uu.nl; m.a.vanhuis@uu.nl

A. D. Sontakke
Condensed Matter and Interfaces, Debye Institute
for Nanomaterials Science
Utrecht University
Princetonplein 5, Utrecht 3584 CC, The Netherlands

 The ORCID identification number(s) for the author(s) of this article can be found under <https://doi.org/10.1002/adfm.202106450>.

© 2021 The Authors. Advanced Functional Materials published by Wiley-VCH GmbH. This is an open access article under the terms of the Creative Commons Attribution License, which permits use, distribution and reproduction in any medium, provided the original work is properly cited.

DOI: 10.1002/adfm.202106450

was also used as a substrate to epitaxially grow unidirectional WS₂ using a multistep metal-organic CVD growth process.^[14] In another approach, metal substrates or inert or insulating substrates were used instead, with the advantage of metal that it can catalytically promote the reaction from the precursor.^[31,32]

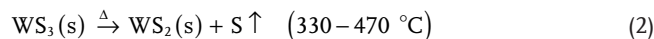
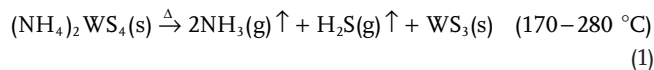
High spatial and temporal resolution by in situ transmission electron microscopy (TEM) provides real-time monitoring of various physical and chemical processes including, growth,^[33–36] phase transformations,^[37–40] sublimation,^[41–47] and electron beam induced modifications.^[48–50] The in situ TEM technique is extensively used to capture dynamics of processes in TMDs as well.^[51–55] In particular, in situ edge engineering in 2D TMDs,^[53] in situ TEM studies of phase transformations of CoSe₂,^[56] PdSe₂,^[57] PtSe₂,^[58] and SnS₂,^[59] and the in situ TEM study of mechanical properties of TMDs,^[60] have been investigated. In situ TEM growth of MoS₂ through thermolysis of ammonium tetrathiomolybdate (NH₄)₂MoS₄ (ATT) was observed on the SiN_x membrane of the heating chip^[61,62] and a Ni deposited heating chip.^[63] Electron beam-induced crystallization and reconstruction of amorphous MoS₂ into crystalline MoS₂ were also studied through atomic scale in situ TEM.^[64] In situ TEM was employed on WS₂ layers as well, through the fabrication of atomically thin nanowall patterns^[28] and atomic-scale localized thinning of 2D WS₂ layers.^[55] Vertical layers of WS₂ were grown in an in situ TEM experiment through thermolysis of K₂WS₄ precursor,^[65] but a detailed understanding of the growth of horizontal WS₂ layers was not reported yet and is still lacking.

In this work, we use in situ TEM heating with the combination of thermolysis of (NH₄)₂WS₄ inside TEM on SiN_x membrane and metal (Pt and Au) substrates, to observe real-time the consequent crystallization and growth behavior of WS₂. We show that the vertical layers of WS₂ grew on thick precursor areas on the SiN_x membrane at lower growth temperatures (450 °C), while horizontal growth of WS₂ layers was observed at thin precursor areas through crystallization of smaller particles at higher temperatures (650 °C). The grain size of WS₂ layers increased via different growth mechanisms including merger of nanograins, at elevated growth temperature (800 °C). The growth of WS₂ horizontal layers was much enhanced on both the Pt and Au deposited heating chips. Twisted layers of WS₂ formed different moiré patterns depending on the twist angle on metal substrates, through altered mobility of interfaces. Raman spectroscopy and ex situ experiments on SiN_x membrane and metal substrates validated the in situ TEM growth. These in situ TEM results can be used to adjust the growth parameters during the thermolysis to design WS₂ materials for applications in catalysis and electronics.

2. Results and Discussion

2.1. Thermolysis of Ammonium Tetrathiotungstate

The growth dynamics of WS₂ were investigated using in situ TEM experiments in which a single solid-state precursor, (NH₄)₂WS₄ (ATT) was heated using an in situ heating holder. It has been reported in previous research that the thermal decomposition of ATT in an inert atmosphere (N₂ ambience) produces crystalline WS₂ through the following steps:^[24,25,66]



The growth of crystalline WS₂ through thermolysis of ATT is less complex as there is no need for a sulfurizing atmosphere, which makes it straightforward to prepare WS₂ for use in applications. Few-layer-thin, large area, and continuous films of WS₂ have been synthesized via the spin-coating method using this precursor which showed good performance in electronic applications comparable to the crystalline WS₂ grown via CVD through sulfurization of WO₃.^[26] The CVD produces large crystals with uniform thickness, whereas in thermolysis of ATT precise control over the growth is lacking. Despite this drawback, the ATT thermolysis route is very viable as it does not require specialized equipment and likely can be easily scaled up, while it provides a great advantage to the investigation by in situ TEM experiments to observe the growth of WS₂ during the thermal decomposition of this single solid-state precursor, which also provides the opportunity to fine-tune this synthesis route.

2.2. In Situ TEM Growth of WS₂ on SiN_x Membrane

The samples for the in situ TEM experiments were prepared by drop-casting of ATT in ethanol solution onto a ≈30 nm thick SiN_x membrane of a TEM heating chip and drying in the air where islands of ATT are formed having different thicknesses. The heating chip is then inserted into the TEM column with a controlled heating setup. Figure S1, Supporting Information shows a schematic of the process of drop-casting of ATT on the heating chip and the introduction of a chip in the TEM column. In the first step, the chip was heated from room temperature to 100 °C and kept for 10 min to remove any residues from the solvent (see Figure S2, Note S1, Supporting Information for more details). The temperature was then increased to 900 °C in steps of 25 °C and the changes were monitored at each stage by holding the temperature for few minutes (more details on sample preparation and experiments are provided in the Experimental Section).

Figure 1 presents the short story of the growth of both vertically oriented and horizontal layers of WS₂. As mentioned above, during sample preparation, ATT islands of varying thickness were formed on the windows of the chip. This was mainly divided into thick and thin precursor parts, where a thick bunch of ATT forms the thicker parts and the relatively thin and smaller islands form the thin precursor parts. Figure 1a shows a thick precursor area at room temperature with dark contrast in the image. The absence of any visible lattice fringes and the diffuse ring without any sharp structures is also evidenced by the corresponding fast Fourier transform (FFT) in the inset, which confirms the amorphous nature of ATT at room temperature. Inspection of the as-deposited sample under the electron beam did not lead to significant changes at room temperature (see Figure S3, Supporting Information). Similar large areas with dark contrast and relatively large thicknesses were observed on different parts of the same window and on other windows of the heating chip.

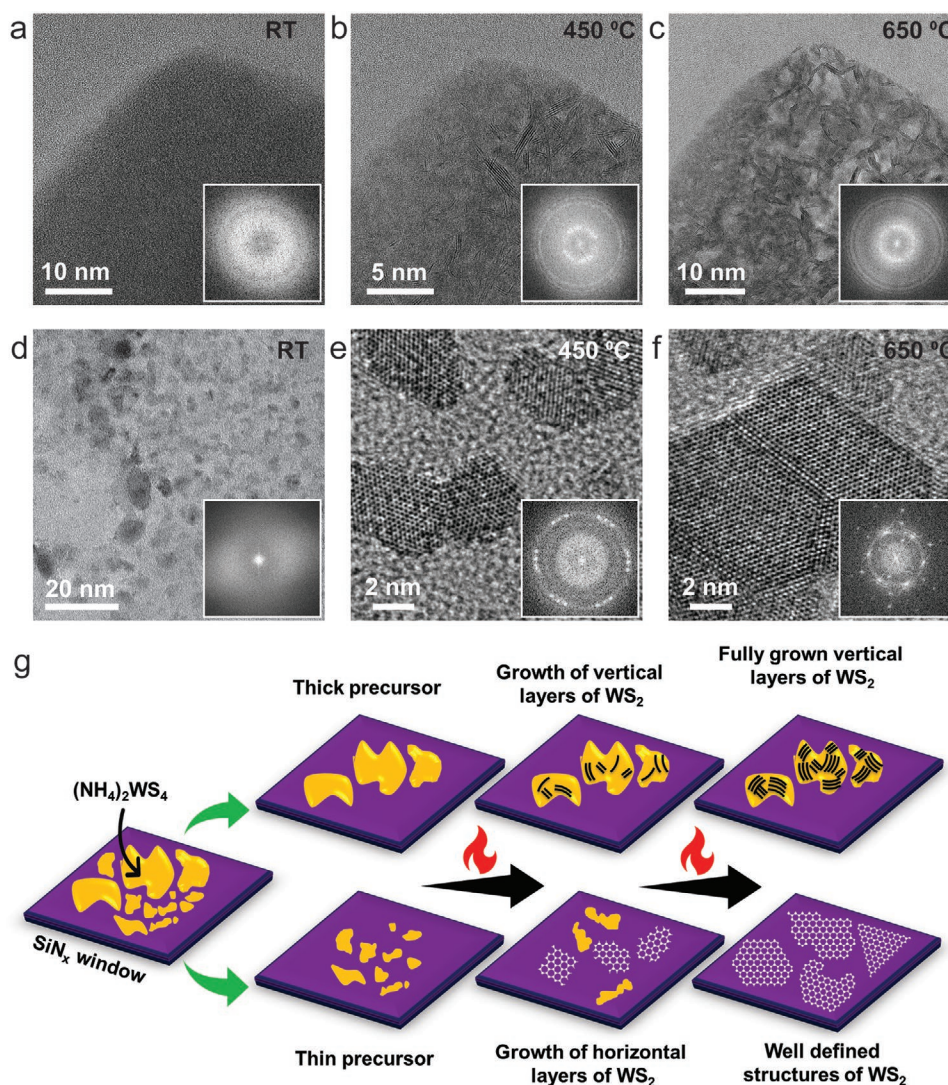


Figure 1. Evolution of vertical and horizontal structures of crystalline WS₂ during in situ TEM heating of ATT precursor. Bright-field TEM images showing: a) Pure ATT precursor, amorphous at room temperature with no fringes in the image. b) Initiation of conversion of the amorphous precursor at a thick area, into vertically oriented WS₂ nanosheets at 450 °C. c) Fully grown clusters of vertical layers of WS₂ at 650 °C. d) Thin precursor area at room temperature with smaller particles and is amorphous in nature. e) Crystallization of smaller particles to crystalline domains with hexagonal structure at 450 °C. f) Larger horizontal structures with sharp edges formed by the merger of nanograins at 650 °C. Insets in (a–f) are fast Fourier transforms (FFT) of the images. Diffuse ring in the FFT patterns (a,d) shows the amorphous nature of the ATT precursor at both thick and thin areas. The thermal evolution of ATT to polycrystalline WS₂ reflects from the bright, sharp, and intense rings in FFT of (b,c,e,f) corresponding to the different lattice fringes of WS₂. g) Schematic illustration of the evolution of polycrystalline WS₂ through thermolysis of ATT precursor, showing a growth of vertical layers and horizontal structures with heating at thick and thin precursor areas, respectively.

Upon increasing the temperature from room temperature in steps of 25 to 450 °C, the first signs of growth of polycrystalline WS₂ were observed with equally spaced (002) crystal fringes on top of an amorphous precursor. These fringes correspond to vertically oriented layers of WS₂, which are observed on-edge in the TEM. At 450 °C, a number of these vertical slabs started to grow at random positions with the amorphous precursor still surrounding them. The corresponding FFT pattern in the inset of Figure 1b verifies the growth of these vertical slabs with sharp, discrete, and intense concentric rings at the same reciprocal spacing as that of the diffuse ring in Figure 1a (inset). These rings suggest the growth of disordered horizontal

structures at thick areas in small amounts while there is predominantly a growth of vertical layers. With further heating to 650 °C, the vertical clusters grow in number, converting most of the precursor into vertical layers standing upright on the SiN_x membrane.

In contrast to the thick areas, the thin areas consist of smaller and thin particles at room temperature showing relatively less contrast in the TEM images as shown in Figure 1d. These particles evolve into horizontal domains displaying a hexagonal crystal structure when increasing temperature to 450 °C. As shown in Figure 1e, each particle can be seen to grow with a hexagonal structure and having a random shape. With heating

at 650 °C, these particles become bigger with finely sharp crystal facets (shown in Figure 1f). The FFT in the inset of Figure 1d depicts the amorphous ATT with a diffuse ring which converts to the sharp and intense ring and bright spots correspond to different lattice fringes of WS₂ with increasing temperatures of 450 and 650 °C (Figure 1e,f). This indicates that the average nearest-neighbor distances in the amorphous material are similar to the well-defined nearest-neighbor distances in crystalline WS₂. The schematic illustration shown in Figure 1g represents the evolution of both vertical and horizontal structures of WS₂ at various stages. As depicted in the schematic, with continued and increased heating, more and more vertical clusters and horizontal structures grow in numbers at thick and thin precursor areas, respectively. Details on both types of growth processes are discussed in the following sections.

The first signs of the crystallization of the amorphous ATT precursor during thermolysis appeared as vertically oriented layers of WS₂. Snapshot frames from a movie recording (Movie S1, Supporting Information) captured at 400 °C, in Figure 2a, shows layer-by-layer growth of vertical layers of WS₂ to form clusters consisting of a few layers that are mutually equally spaced. Figure 2a shows an amorphous region of the precursor with slightly visible edge steps of two vertical layers at 400 °C, which is the initiation of the growth of vertical layers on top of the amorphous precursor. In the next frame, two grown vertical layers surrounded by the amorphous precursor with a step edge of another layer can be observed.

It has been reported previously that for vertical growth of MoS₂, the step edges of previous layers are energetically favorable for initiating the growth of the next layer,^[61] which we have noticed in this case as well. A close look at these frames reveals that the vertical layers are growing next to each other and matching the size of existing ones to form a cluster of vertical slabs (≈8 layers) of WS₂ at 450 °C. In the subsequent frames, these vertical layers grow to similar lengths while maintaining equal interlayer spacing. With continued heating, monomers are attached to the existing clusters and grow with the number of vertical slabs to some extent. Figure 2b–e shows one of the examples where the amorphous region is kept under continuous electron beam exposure during heating. The thick precursor with dark contrast and no features at room temperature can be seen in Figure 2b, which evolves into the few vertical layers at 400 °C (Figure 2c). With increasing temperature, the number of vertical layers evolves as clusters at 650 °C that are covering almost all of the precursor area (Figure 2e). From our methods and experiments, we do not have exact information on the atomic structure of the base of the vertical layers, but there are several reports that provide interesting concepts on the base of the nanowalls of vertically oriented 2D materials.^[18,67–70] According to the study done on MoS₂,^[61] during the beginning of the crystallization, vertically oriented layers have a lower formation energy (i.e., a low interface energy with the SiN_x membrane) in comparison to horizontally oriented layers.

These growth patterns were found everywhere on the heating chip, also in areas not previously exposed to the electron beam. This shows the negligible effect of the electron beam and local heating induced by the electron beam, on the growth of these structures. Similar vertical structures observed in areas where the sample was not continuously exposed to the electron beam

are presented in Figures S4–S6, Supporting Information, and described in Notes S2,S3, Supporting Information. It has been reported that the metal (Mo or W) seed layer thickness plays a critical role in the growth orientations of MoS₂ or WS₂,^[18] whereas in the present study we show that the thickness of the ATT precursor is a key factor in the growth of vertical or horizontal structures of WS₂. The interlayer spacings observed by high-resolution TEM (Figure 2f) and by high-angle annular dark-field scanning TEM (HAADF-STEM) (Figure 2h) imaging, are 0.62 and 0.6 nm, respectively (in Figure 2g,i) similar to the value in bulk WS₂. These vertical structures grew in size (i.e., through an increase in the number of layers in a cluster) with continuous heating. Figure 2j–m shows TEM images captured at 450, 500, 650, and 800 °C, respectively. With the increase in temperature from 450 °C, the number of layers started to increase in the vertical cluster, leading to a larger lateral dimension of these clusters. As discussed above, the in-plane length of the vertical layer matches the previously grown layers by growing next to them also when more layers are added to the cluster. The statistical histograms are shown in Figure 2n–q for the corresponding TEM images at 450, 500, 650, and 800 °C and provide the average number of layers ≈4 ± 2, 5 ± 1, 6 ± 2, and 8 ± 3 for each temperature, respectively. This confirms that the size of the vertical clusters increases with temperature to 800 °C, but further heating does not add any number of layers to the existing cluster, thus keeping the same cluster size above 800 °C. At temperatures of 650 and 800 °C, a maximum of 15 and 18 layers are observed in an individual cluster. In the case of MoS₂ growth, it has been observed that the formation of a new layer is energetically more favorable than the elongation of existing layers,^[61] which we have noticed in the growth of vertical layers of WS₂ as well. This can be seen from the images at higher temperatures showing bigger cluster sizes and while having limited in-plane lengths of the vertical layers inside the clusters. It is possible to grow only vertical layers of WS₂ by controlled deposition of thick precursor as presented in Figure S7, Supporting Information.

Horizontal growth, in which WS₂ layers grow in planar direction with their basal plane parallel to the SiN_x membrane of the heating chip, was observed at thin precursor areas. As shown in Figure 3a, the ATT precursor also formed thin areas containing only small and thin particles compared to the thick parts. The TEM image in Figure 3a depicts the randomly shaped precursor particles with low contrast at room temperature after drop-casting ATT precursor onto the heating chip. The lack of any lattice fringes at room temperature reflects the amorphous nature of the ATT precursor. At the onset of heating, these small and thin amorphous particles start to show modifications with signs of crystallization. Notably, at 400 °C, hexagonal crystallites of different crystal orientations form at thin precursor areas all over the SiN_x membrane. Figure 3b shows one of the areas shown in Figure 3a where the precursor has transformed into crystallites after heating to 400 °C. These crystallites that are exposing (100) crystal planes are found in different orientations while being in contact with each other, as can be seen in Figure 3b. With increasing temperature to 450 °C, these particles go through crystal orientations to align and match the (100) planes, forming a single crystal through coalescence and oriented attachment^[71] as

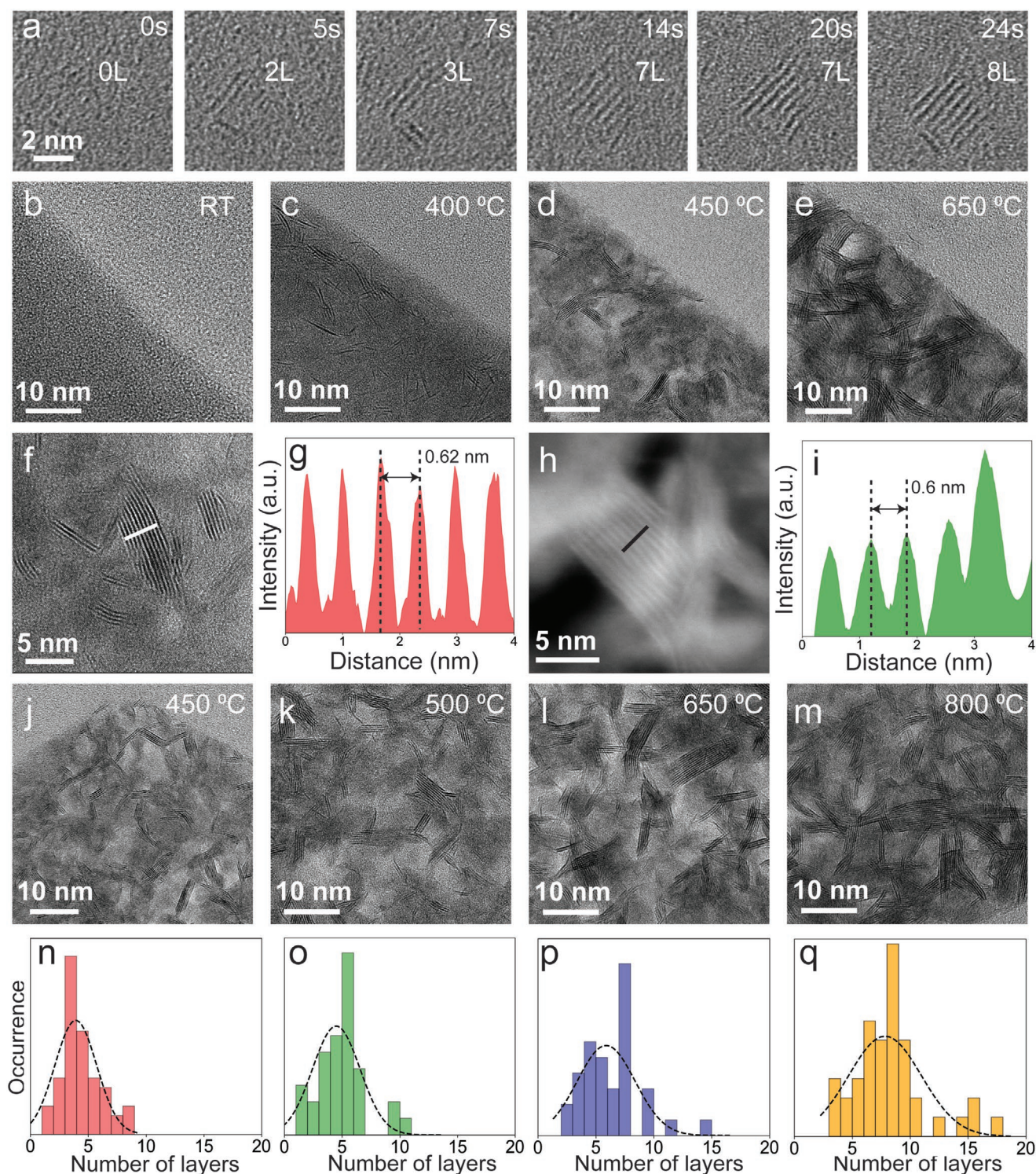


Figure 2. Growth of vertically aligned layers of WS₂. a) Snapshot frames are taken from Movie S1, Supporting Information showing the dynamics of layer-by-layer vertical growth of WS₂ layers. b–e) Thick precursor area under continuous electron beam exposure during thermolysis of ATT: (b) Amorphous ATT precursor with dark contrast at room temperature in the TEM image. (c) Initiation of growth of vertical layers at 400 °C standing upright on the SiN_x membrane. (d,e) Vertical clusters of WS₂ grown with more layers attached to the existing ones at 450 and 650 °C. f,h) Magnified TEM and STEM images of vertical layers. g,i) Intensity line profiles along the lines indicated in panels (f) and (h), from which an interlayer spacing of ≈0.6 nm was measured for both cases. j–m) TEM images of vertical clusters and n–q) histograms showing the number of layers in vertical clusters observed at 450, 500, 650, and 800 °C, respectively.

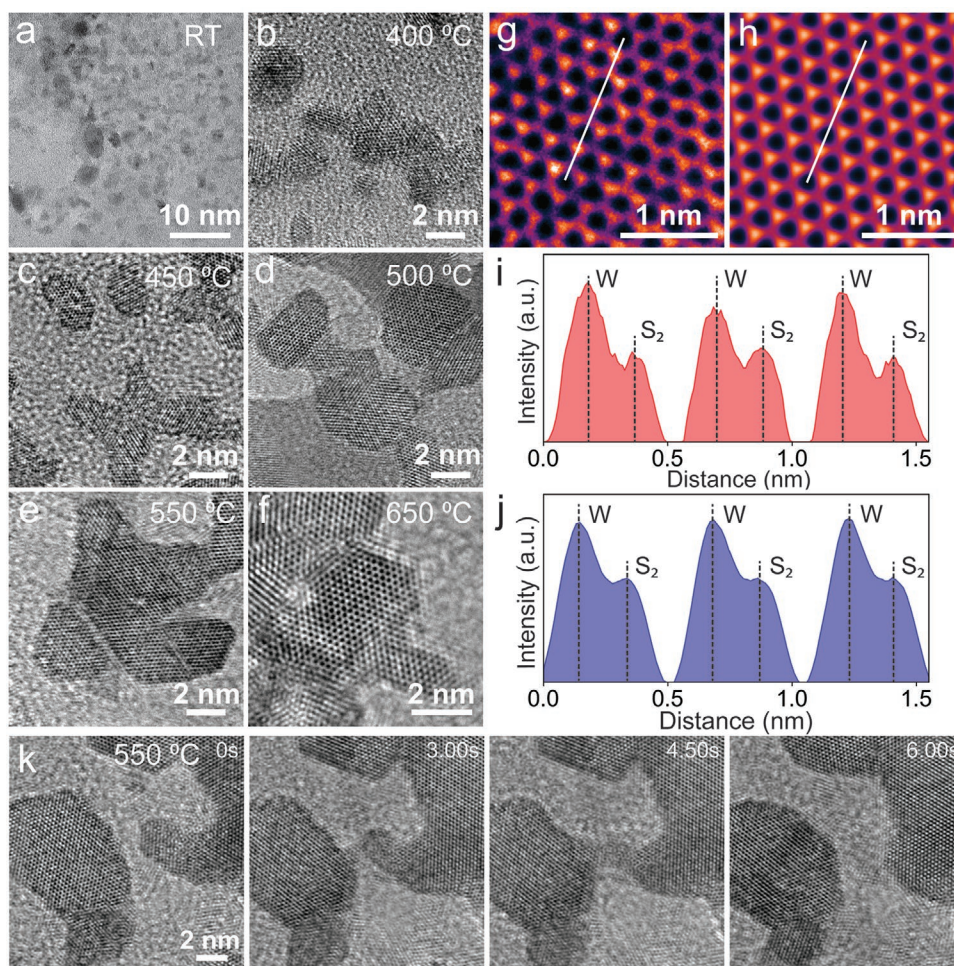


Figure 3. Horizontal growth of WS₂ layers. a) Thin precursor area with smaller randomly shaped and thin particles at room temperature. b) Crystallization of thin precursor particles at 400 °C. c) Hexagonal crystal lattice formation at thin precursor particles at 450 °C. d,e) Formation of bigger particles by merging nanograins at 500 and 550 °C, respectively. f) Quasi hexagonal horizontally oriented nanoflakes with crystal facets exposed at the edges at 650 °C. g) High-resolution TEM image of the hexagonal structure of a horizontal WS₂ layer. h) Simulated TEM image of the basal plane oriented WS₂ layer. i,j) Intensity line profiles of the lines drawn on the TEM images in (g) and (h) respectively. k) Snapshot frames from Movie S2, Supporting Information showing the fusion of nanograins at 550 °C. The images in (g,h) are applied with the GEM LUT effect in ImageJ software for better display purposes.

shown in Figure 3c. The randomly shaped crystallites show a clear hexagonal crystal structure at 450 °C as in Figure 3c. The smaller nanograins that are formed at 400 °C, fuse into a single crystallite as can be clearly seen from Figure 3c. A similar type of growth was observed in one another experiment carried out with identical conditions and this is shown in Figure S8a–c, Supporting Information.

As the temperature reached 400 °C, crystallites of WS₂ exhibiting (100) interplanar spacings and found in different crystal orientations were formed. All these crystallites can be seen to be in contact with each other in Figure S8a, Supporting Information. As mentioned above, these particles also went through rotations where crystals orient to align and match (100) planes to form a big single particle as shown in Figure S8b, Supporting Information, at an increased temperature of 450 °C. At 500 °C, all these particles result in large, well-faceted crystals through coalescence and 2D crystal fusion (Figure S8c, Supporting Information). This growth mechanism is referred to as oriented attachment,^[71–73] wherein the crystals with different

orientations approach each other, rotate to align crystal planes, and after attachment and further relaxation form a single crystallite.

When the temperature was increased further to 500 °C, small flakes merged and formed bigger flakes as shown in Figure 3d. At 550 °C, these big flakes started to form well-faceted edges through mass redistribution, and at 650 °C it resulted in a quasi-hexagonal structure with well-faceted edges. Figure 3k shows one of the examples through a sequence of stills from Movie S2, Supporting Information, wherein nanograins merged to form bigger flakes at 500 °C. A part of the grain from the right side in Figure 3k approached another grain at the left and merged with it, making it larger. This process, where large crystals grow at the expense of small ones, is generally known as Ostwald ripening^[74] and is observed in coexistence with other growth mechanisms. One more example of this type of growth is shown in Figure S8d–f, Supporting Information, where already crystallized particles merged and formed bigger ones at 550 °C with facet development at the edges at 650 °C. With increasing

temperature, the degree of crystallization increases as the number of defects is lowered during the growth, that is, concurrently a ripening process is taking place. A high-resolution TEM image of the hexagonal honeycomb crystal structure recorded from one of the fully grown horizontal flakes is shown in Figure 3g. The intensity line plot profile in Figure 3i corresponds to the line drawn in Figure 3g, which shows a 2H (trigonal prismatic) type of WS_2 . Figure 3h depicts the simulated TEM image and a line profile (Figure 3j) for W and S atoms in WS_2 . The experimental and simulated TEM images agree well, which confirms that the grown material is 2H WS_2 . From our in situ TEM data, the edge terminations of flat WS_2 layers could not be resolved in detail. However, scanning tunneling microscopy studies on the edge termination of MoS_2 ,^[75] which strongly resembles the WS_2 lateral structures, have previously shown preferential S-termination at the horizontal edges.

Figure S9, Supporting Information shows yet another example wherein already crystallized grains are nearing, attach, and form a new, big crystal. Specifically, the grains indicated by 1 and 2 in Figure S9a, Supporting Information at 550 °C approached each other, both having hexagonal lattices with different orientations. In Figure S9d, Supporting Information these grains attach and form a neck at the point of attachment (indicated by the arrow), which is followed by complete attachment in Figure S9f, Supporting Information whereby a new and big grain was formed with the same crystal lattice. In another example in Figure S10, Supporting Information (from Movie S3, Supporting Information) and Figure S11a–d, Supporting Information, small grains simply approached each other and fused at 550 °C. The grains with sharp edges which are formed by the facet rearrangements can be seen to merge at 650 °C in Figure S11e–h, Supporting Information. Snapshot frames from a movie with edge reconstructions of WS_2 are shown in Figure S12, Supporting Information. A big area where the whole growth process could be followed is shown in Figure S13, Supporting Information, where a relatively big area of the thin precursor was monitored during heating from room temperature to 650 °C. The amorphous precursor at room temperature (Figure S13a, Supporting Information) was heated to 500 °C, at which temperature it formed randomly shaped crystallized grains (Figure S13b, Supporting Information), with slightly different contrast in the TEM image. An HR-TEM image of one of these grains is shown in Figure S13e, Supporting Information, showing hexagonal crystal lattices of WS_2 . Furthermore, an increase in temperature to 650 °C resulted in the darker and bigger grains with fine edges (attributed to form by facet development) (Figure S13c, Supporting Information). An HR-TEM image of one of these grains shown in Figure S13f, Supporting Information, which was captured from the same area in Figure S13e, Supporting Information, confirms the merging of small grains and the formation of sharp boundaries. STEM-EDS (energy dispersive X-ray spectrometry) elemental maps in Figure S13h,i, Supporting Information suggest the uniform distribution of S and W in these grains with a 1:2 ratio for W and S.

Another example of the formation of a large flake of WS_2 is shown in Figure S14, Supporting Information where the merged small grains became one large flake through grain boundary migration. During the merging of different grains, a

polycrystalline nanosheet was formed, which can be best described as a large flake with grain boundaries between the smaller crystalline domains. It has been reported that in 2D crystals like WS_2 , dislocations exist on the surface and can interact with the surface atoms.^[76] Mobile S atoms can interact with the dislocation cores and can form derived dislocation structures through migration processes that involve a rearrangement of W and S atoms around the defect, which in turn leads to grain boundary reconstruction.^[76] In the present case as shown in Figure S14, Supporting Information, thermally induced grain boundary migration occurred, resulting in a large single crystalline flake. Different grains are indicated by numbers and grain boundaries between them are indexed by the colored dotted lines in Figure S14a, Supporting Information. While the temperature was kept at 700 °C, all these separate grains disappeared, and a single crystalline large flake (indicated by a white dotted border in Figure S14d, Supporting Information) was formed by migration of the grain boundaries to the surface. A similar type of process was observed at a smaller scale and is shown in Figure S15, Supporting Information. As depicted in Figure S15a, Supporting Information, the configuration consisted of six different grains as indicated by the different colors. After few minutes of heating, these grains vanished and a new relatively large single-crystalline flake was formed (shown by the yellow color in Figure S15d, Supporting Information). The white arrow in Figure S15b,c, Supporting Information indicates the direction of propagation of grain boundaries. FFTs shown in Figure S15e–h, Supporting Information confirm the transition from multi-grained flake to single-crystalline flake. Fairly large flakes of WS_2 were obtained through thermolysis of ATT precursor inside TEM and are shown in Figure S16, Supporting Information. The HR-TEM image and FFT in Figure S16b,c, Supporting Information confirm the single-crystalline nature of the WS_2 flake. Further heating of these WS_2 flakes to 900 °C resulted in the transformation process in which WS_2 transformed into elemental metallic tungsten (W). As shown in Figure S17, Supporting Information, the hexagonal structure of WS_2 transformed to the cubic crystal structure of W at 900 °C. The time-series images (frames from Movie S4, Supporting Information), shown in Figure S17a–d, Supporting Information depict how the WS_2 structure breaks into metallic W. The interplanar spacings for WS_2 and W structures were found to be 0.27 and 0.23 nm for (100) and (110) planes, respectively when imaged through the [001] zone axis. Therefore, the WS_2 layers had transformed into body-centered cubic (bcc) tungsten (W). The corresponding FFTs are shown in the inset of Figure S17e,g, Supporting Information. Intensity line plot profiles for WS_2 and metal W are shown in Figure S17f,h, Supporting Information, respectively, and the intensity line profile for metal W shows the disappearance of S peaks in the cubic crystal structure which indicates the removal of S atoms.

2.3. Ex Situ Growth of WS_2 on SiN_x Membrane

The thermal evolution of WS_2 through thermolysis of solid-state precursor, as described above, has been disclosed through in situ TEM experiments. These experiments were carried out

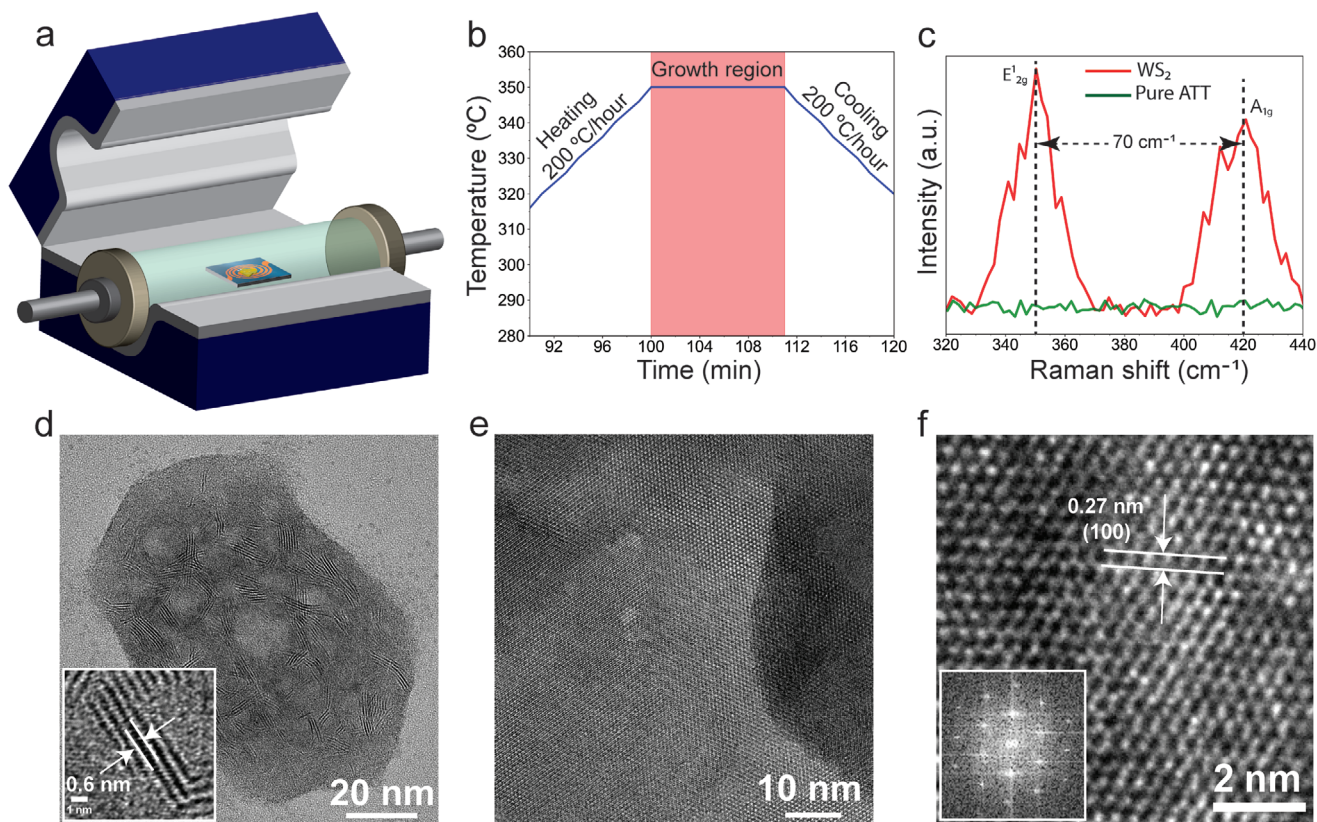


Figure 4. Ex situ growth of WS₂ structures. a) Schematic representation of vacuum oven used for the ex situ experiments. b) Temperature profile for the vacuum oven heating including a horizontal profile of 10 min at 350 °C to promote the growth. c) Raman spectra of ATT precursor and ex situ grown WS₂ structures recorded at room temperature. d) Growth of vertical layers in ex situ experiment at one of the parts of ATT precursor with a magnified view of vertical layers in the inset. e) Vacuum oven growth of horizontal structures of WS₂ at 350 °C. f) HR-TEM image captured from one of the horizontal structures with corresponding FFT in the inset.

on a local area of the TEM heating chip which is not necessarily representative of the thermal evolution of large areas of the sample. To confirm the global growth process, and to validate in situ TEM results, we have conducted ex situ experiments with a large amount of ATT precursor within a vacuum oven (see the Experimental Section for details). The schematic of the vacuum oven is depicted in **Figure 4a**, with a quartz tube accommodating ATT precursor in the form of powder on a TEM heating chip that is placed at the center of the oven which was evacuated down to a pressure of 2 mbar. The temperature profile for heating in the vacuum oven is shown in **Figure 4b** (full temperature profile is shown in **Figure S18a**, Supporting Information). As shown in **Figure 4b**, the ATT precursor in the form of powder, drop cast on the TEM heating chip was heated at 350 °C for 10 min.

This is referred to as the growth period in **Figure 4b** indicated with the red patch, in which both vertical and horizontal WS₂ structures grew. As shown in **Figure 4c**, Raman spectra of pure ATT precursor before heating and after ex situ growth of WS₂ powdered samples were recorded at room temperature with laser excitation at a wavelength of 532 nm. No Raman signal was observed for the pure ATT precursor and the two characteristic first-order optical modes of E_{2g}¹ (in-plane vibrational mode) and A_{1g} (out-of-plane vibrational mode) at 350 and

420 cm⁻¹, respectively, are observed for the ex situ grown WS₂ samples.^[16] A frequency separation of ≈70 cm⁻¹ between E_{2g}¹ and A_{1g} modes^[30] at 532 nm laser excitation may perhaps be the spectral fingerprint of a few-layer thin WS₂. TEM images of both the powdered sample and the sample on a heating chip are recorded and are presented in **Figure 4d–f**. Bath sonication was used to exfoliate powdered samples before drop-casting them onto the TEM chip. **Figure 4d** shows one of the examples of ex situ prepared powdered samples, wherein vertically oriented layers can be seen. A magnified view of the vertical layers with an interlayer spacing of ≈0.6 nm is shown in the inset of **Figure 4d**. A detail of a horizontal WS₂ layer is shown in **Figure 4e** and depicts thickness-dependent contrast in the TEM image with a different number of horizontal layers. An HR-TEM image showing the hexagonal lattice structure and interplanar spacing of 0.27 nm, corresponding to (100) planes for horizontal 2H-WS₂, along with corresponding FFT in the inset, is shown in **Figure 4f**. EDS elemental mapping for W and S in as grown WS₂ samples are shown in **Figure S18c,d**, Supporting Information for the area shown in **Figure S18b**, Supporting Information. **Figure S18f**, Supporting Information shows WS₂ clusters formed on the heating chip in an ex situ experiment along with HAADF-STEM image and STEM-EDS elemental maps for W and S in **Figure S18g–i**, Supporting

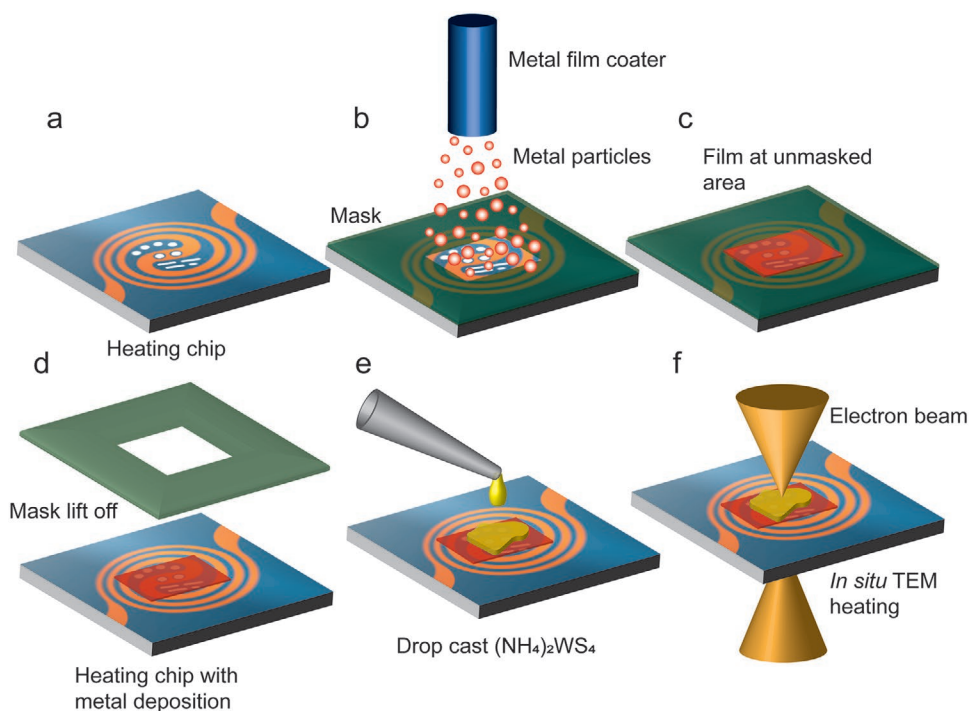


Figure 5. Schematic illustration of deposition of metal (Pt/Au) film onto the TEM heating chip. Panels (a–f) show the subsequent steps in the procedure.

Information, respectively. An EDS spectrum recorded from the powdered samples is shown in Figure S18e, Supporting Information and quantification of EDS data confirms $\approx 1:2$ ratio for as grown WS_2 sample. Thus, both vertical and horizontal growths of WS_2 are observed through ex situ vacuum oven heating of ATT precursor and are in good agreement with our in situ TEM observations. The thick precursor area which grew into the vertical layers of WS_2 (in Figure 4d) was pre-checked using TEM, and images of the area before and after ex situ heating are presented in Figure S19, Supporting Information.

2.4. In Situ TEM Growth of WS_2 on Metal (Pt and Au) Deposited Chips

The in situ TEM growth of both vertical and horizontal structures of WS_2 discussed in the above sections was observed on a chemically inert SiN_x window. Inspired by the metal substrate approach,^[31,32] we have employed metal film deposition on TEM heating chips (see details in the Experimental Section) to observe any structural modifications during thermolysis driven growth of WS_2 . As depicted in Figure 5, two different metal films, platinum (Pt) and gold (Au) with a thickness of ≈ 5 nm were deposited onto the heating chips by applying a mask to the chip, leaving the SiN_x window area unmasked. These metal films were used as a substrate and the ATT precursor was drop cast onto these metal deposited heating chips and subsequently heated inside the TEM to investigate modified, enhanced, or catalytically activated growth. For the heating of ATT precursor onto the metal deposited heating chips, procedures similar to the in situ TEM investigations of growth of WS_2 on the bare SiN_x membrane were followed.

2.5. In Situ TEM Growth of WS_2 on Pt Deposited Chip

The Pt deposited film onto the SiN_x window of the heating chip and the amorphous ATT precursor on top of it can be seen in a TEM image captured at room temperature in Figure 6a. The dark contrast represents ATT precursor and irregular structures with varying contrast depict a ≈ 5 nm thick Pt film. It can be seen that the Pt film is non-continuous with small voids in between Pt particles. With an increase in the temperature, the ATT precursor begins to transform to the crystalline structure, and at 450°C vertical layers of WS_2 grow to display on-edge the (002) layered planes, standing up as shown in Figure 6b. The contrast in Figure 6b changes as the vertical clusters of WS_2 form at different positions on the precursor. Figure 6c shows a magnified view of the area marked with a square in Figure 6b and shows the interlayer spacing of 0.6 nm for WS_2 vertical layers. In a single vertical cluster of WS_2 , 4–9 layers can be seen with Pt film in the background.

Dynamics of the growth of vertical layers during heating were recorded and is shown in Movie S5, Supporting Information. Snapshots from Movie S5, Supporting Information are shown in Figure 6d and the area where the vertical layers grow is indicated with a rectangle. This layer-by-layer growth of vertical layers is identical to the growth observed on the inert SiN_x window as described in the first part, but with a slight increase in the length of layers (see Figure S20, Supporting Information). In the background in Figure 6d, Pt particles are visible which might have played an important role in increasing the lengths of these layers. As this transformation from amorphous precursor to crystalline WS_2 occurs under the electron beam, the effect of illuminating electrons cannot be ruled out. Therefore, the growth of vertical layers of WS_2 on Pt deposited

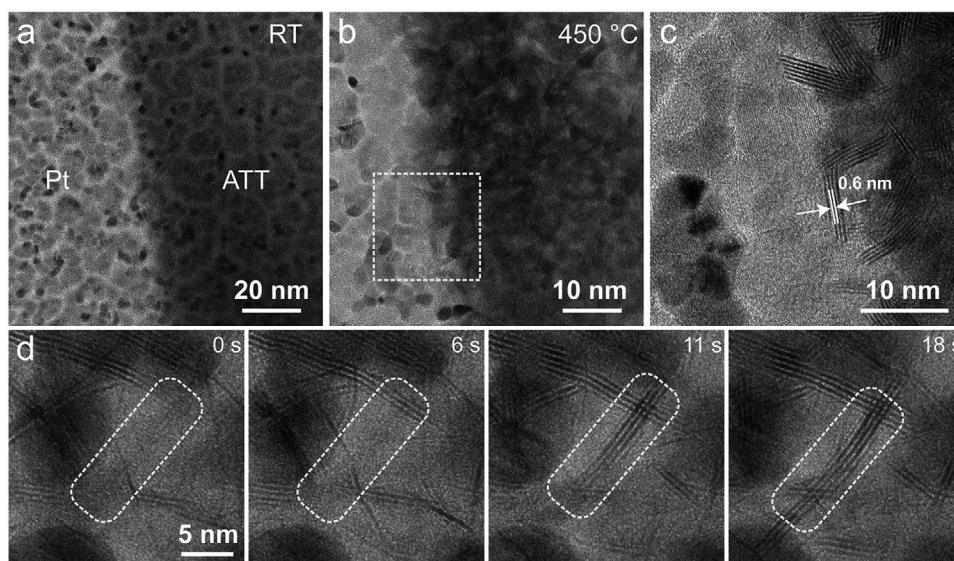


Figure 6. Growth of vertical layers of WS_2 on Pt deposited heating chip. a) Amorphous ATT precursor (with dark contrast) on Pt film (≈ 5 nm) deposited onto the heating chip. b) Growth of vertical layers of WS_2 at 450°C . c) Magnified view of the square marked in (b), with vertical layers visible with an interlayer spacing of 0.6 nm. d) Snapshot frames captured from a Movie S5, Supporting Information, showing the real-time growth of vertical layers of WS_2 on Pt deposited heating chip.

heating chips under the continuous electron beam exposure but also growth at areas where the process was not continuously monitored by the electron beam, are presented in Figures S21 and S22, Supporting Information, respectively. Both these observations show similar growths of vertical layers which in turn suggest a negligible effect of an electron beam on WS_2 growth (details on Figures S21 and S22, Supporting Information are discussed in Note S4, Supporting Information).

Growth of horizontal, basal plane oriented layers of WS_2 was observed on Pt deposited heating chips when the ATT precursor was heated to 650°C . Different stages of WS_2 growth are shown in Figure 7a–d after heating at temperatures of 400 , 450 , 550 , and 650°C . The same precursor area (thin) was monitored during in situ TEM heating to observe various steps of growth. In Figure 7a, the amorphous ATT precursor area is shown with no visible fringes but some developing structures as shown in Figure 7e, which is a magnified view of the square marked in Figure 7a. This does not display any clear crystal structure but the FFT in the inset of Figure 7e shows short-range structural ordering. An increase in the temperature by 50°C leads this structure to organize into domains of hexagons of WS_2 at 450°C as depicted in Figure 7f. The slightly different FFT with bright spots in the inset of Figure 7f suggests the development of the hexagonal crystal structure of WS_2 displaying a few more spots. These hexagons of WS_2 extend with further growth during an increase in temperature to 550°C and show more hexagons with more bright spots in FFT as shown in Figure 7g and the inset, respectively.

An interesting pattern can be seen in Figure 7d which can be recognized as a moiré pattern which is the interference between two layers that are twisted by an angle with respect to each other. A bigger picture of this pattern is shown in Figure S23, Supporting Information with corresponding FFT in the inset. A close look at this moiré pattern (Figure 7h) suggests that the

growth of WS_2 at a thin precursor area leads to the formation of two WS_2 layers on top of each other with slightly different rotations. The FFT in the inset of Figure 7h clearly shows different spots for each layer separated by some angle. To investigate the moiré patterns in detail, the FFT from a clear area with a moiré pattern (Figure 7i) was taken and shown in Figure 7j. The FFT reflects bright spots for both layers of WS_2 and is separated by an angle of 9° as shown in Figure 7j. To elaborate on this, schematic illustrations are shown in Figure 7l,m. Two layers of WS_2 with no mismatch angle (0°) between them would look like a single layer as shown in Figure 7l and if one of the layers is twisted by 9° the pattern would be as shown in Figure 7m which exactly matches the HR-TEM image in Figure 7i. A clear difference between a single layer and bi-layer WS_2 with a 9° twist angle can be seen from Figure 7k, where the moiré pattern with two layers differentiates the single layer of WS_2 . The schematic illustration of this type is shown in Figure 7n with one layer of WS_2 beneath another which is twisted by 9° , which indeed generates the moiré pattern. This is further explained in Figure S24, Supporting Information by taking the FFT of the moiré pattern and forming its inverse FFT (IFFT) filtered image to visualize it better (as shown in Figure S24c, Supporting Information). Applying masks to the bright spots for each layer in the bilayer configuration of WS_2 in FFT, filtered IFFT images of both the layers are separated as shown in Figure S24d,e, Supporting Information. The twist angle of 9° between these two layers (shown in Figure S24e, Supporting Information) creates the moiré pattern.

Thus, on Pt deposited heating chips, bilayer growth of WS_2 was observed and no signs of the formation of platinum sulfides were observed during the in situ TEM heating of the ATT precursor. With the Pt film deposited onto the heating chip, Pt nanoparticles formed and settled at the edges of WS_2 structures during in situ TEM heating as shown in Figure S25, Supporting Information. This was found to take place at different windows

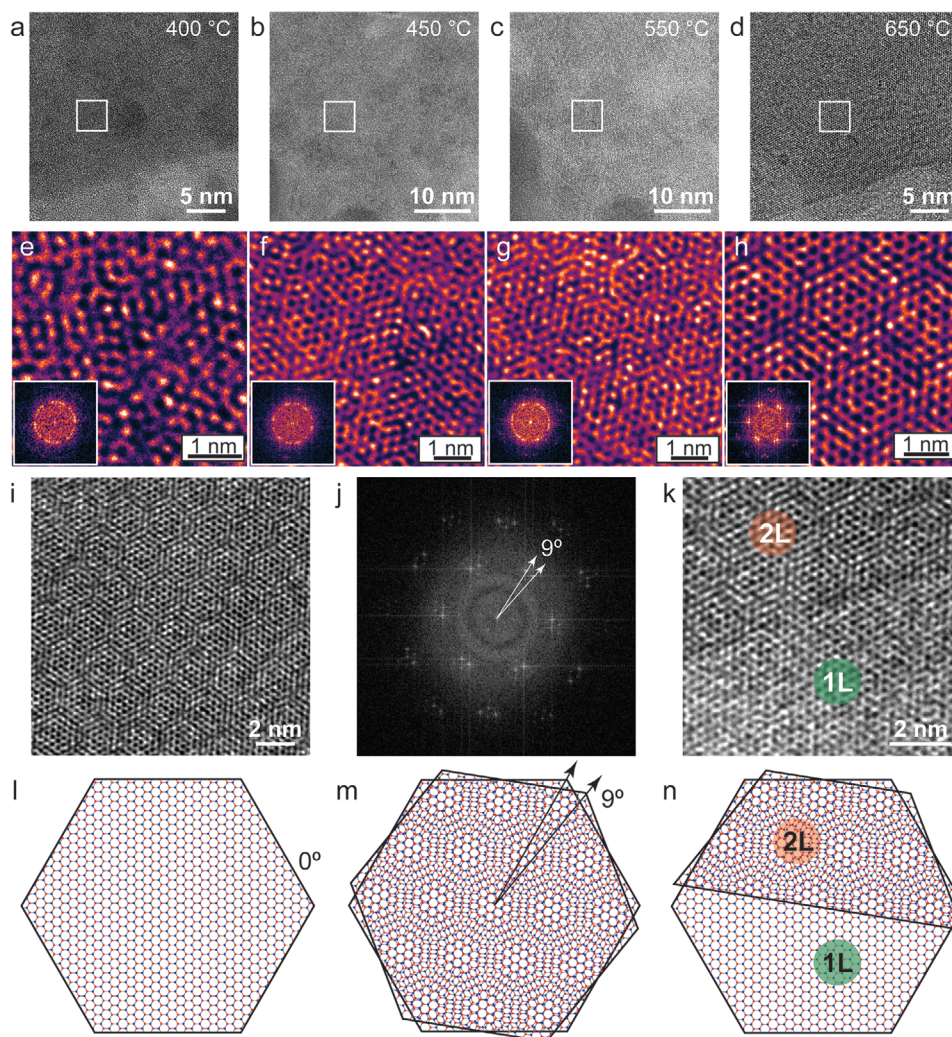


Figure 7. Growth of horizontal WS₂ layers on Pt deposited heating chip. a–d) Different growth stages of horizontal WS₂ layers on Pt deposited heating chip at 400, 450, 550, and 650 °C (all images are from the same area). e–h) Enlarged view of the growth steps from the areas marked with squares in (a–d) and the inset shows corresponding FFTs. All the images are applied with the GEM LUT effect in ImageJ software for better visualization. i) HR-TEM image of moiré pattern formed due to the twist of one WS₂ layer to the other in a stack of two layers. j) FFT of two layers of WS₂ forming moiré pattern and showing twist angle of 9°. k) Two layers of WS₂ mismatched by 9° with moiré pattern and a single layer beneath it with a hexagonal structure. l–n) Schematic representation of two WS₂ layers with a rotation of 0° between them, with a rotation of top layer by 9° to the bottom layer forming moiré pattern and a single (indicated by 1L) and a double layer (indicated by 2L) with moiré pattern, respectively.

of the heating chip with different thicknesses of the precursor. As depicted in Figure S26, Supporting Information, Pt nanoparticles nucleate and aggregate at the edges of thin, medium-thin, and thick precursor areas that are grown to the crystalline WS₂ structures after heating to 800 °C. Thus, Pt deposition over the heating chip provides a metal substrate that acts as a catalyst in the growth of WS₂ layers with growth limited to two layers, and which also plays role in producing Pt-WS₂ hybrid structures. Furthermore, a Pt deposited SiN_x window of the heating chip after heating to 800 °C with WS₂ structures is shown in Figure S27a, Supporting Information. The HAADF-STEM image (Figure S27b, Supporting Information) and EDS elemental maps for Pt, W, and S recorded from the same area (Figure S27c–e, Supporting Information) suggest the growth of WS₂ and aggregation of Pt particles at the edges of WS₂ structures to form Pt-WS₂ hybrid structures. Very thin WS₂ layers are shown in Figure S27g, Supporting Infor-

mation and EDS line scans for WS₂ layers without and with Pt particles (with 1:2 ratio for W and S in both the cases) are shown in Figure S27l,m, Supporting Information, respectively. This confirms the growth of fairly thin WS₂ layers on Pt deposited heating chips along with the hybrid Pt-WS₂ structures.

2.6. In Situ TEM Growth of WS₂ on Au Deposited Chip

The growth of WS₂ layers on Au films is studied extensively in ex situ experiments (in CVD), where reusable Au foils were used as a substrate to grow large area, high quality, and uniform monolayer WS₂.^[31,32] In some other studies, Au droplets were used as nucleation centers to grow monolayer and single-crystal WS₂.^[77] As reported earlier^[31] Au doesn't react with the sulphur to form sulphides at higher temperatures,

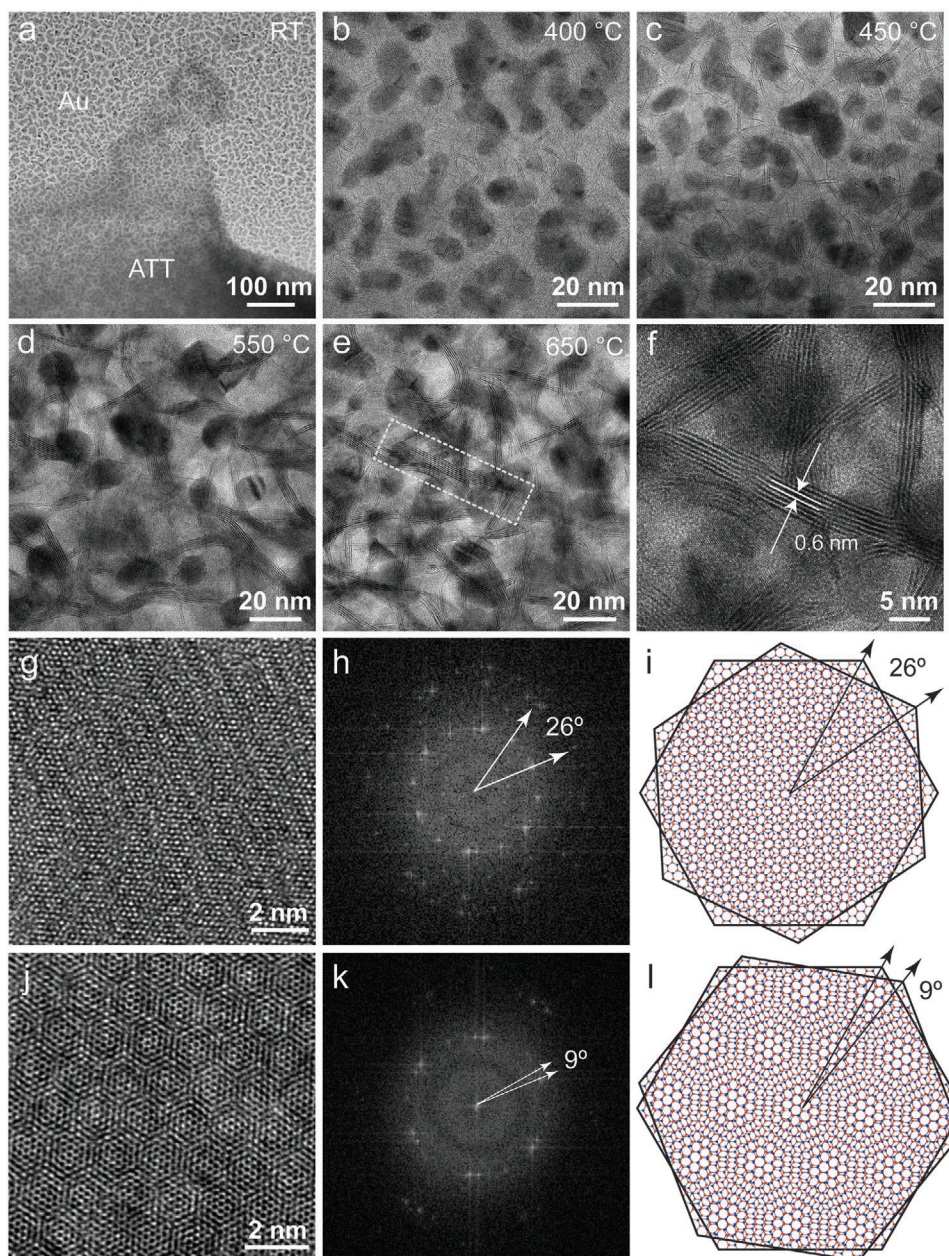


Figure 8. Growth of vertical and horizontal WS_2 structures on Au deposited heating chips. a) Amorphous ATT precursor onto the Au deposited heating chip at room temperature. b–e) Growth stages of vertical layers of WS_2 at 400, 450, 550, and 650 °C, respectively (Au particles are visible in the background). f) High-resolution TEM image of the rectangle marked in (e) with an interlayer spacing of ≈ 0.6 nm. g, j) The moiré patterns are formed by a twist of two WS_2 layers (on the Au deposited chip) by 26° and 9° respectively. h, k) FFTs of the HR-TEM images in (g, j), with angle representation of 26° and 9° respectively for the bright spots appearing due to the overlay of two layers of WS_2 . i, l) Schematic illustration of the moiré patterns formed by twist angles of 26° and 9° between two layers of WS_2 .

and low solubility of W in Au (<0.1 at% at 800 °C) avoids multilayer growth of WS_2 through a self-limited surface catalytic process. By considering these advantages of an Au substrate, we also deposited an Au film onto the TEM heating chip as shown in Figure 5 followed by a drop-cast of ATT precursor (Figure 8a with amorphous ATT precursor and Au film in the background) to further observe the growth of WS_2 . As mentioned in the earlier sections, the growth of vertical WS_2 layers appears first on thick precursor areas after heating to

400 °C as shown in Figure 8b with few short in-plane length of vertical layers. With an increase in temperature, these vertical layers grow in size (number of layers in a cluster) and in in-plane length as shown in Figure 8c–e, at temperatures of 450, 550, and 650 °C, respectively. The length of vertical clusters in the Au deposited chip is the longest one compared to the growth on SiN_x window and on Pt deposited heating chip. An interlayer spacing of ≈ 0.6 nm (Figure 8e) is in good agreement with the interlayer spacing in bulk WS_2 .

One more example of the dynamics of vertical growth of WS₂ layers on an Au deposited chip is depicted in Figure S28, Supporting Information. Images were recorded at different temperatures (400, 450, 500, 550, 600, and 650 °C) during the growth process and are shown in Figure S28b–g, Supporting Information. The growth was observed on the windows on the heating chip that were not continuously illuminated by the electron beam during heating (Figure S28i–l, Supporting Information). The EDS measurements (Figure S28n–p, Supporting Information) suggest a uniform distribution of W and S in the WS₂ with irregularly shaped Au particles in the background.

A different type of moiré pattern was observed during the growth of horizontal layers of WS₂ on Au deposited chip and is shown in Figure 8g. The analysis of bright spots in FFT of this type of moiré pattern suggests a 26° mismatch between two layers of WS₂ (as shown in Figure 8h). The schematic displayed in Figure 8i illustrates the formation of the moiré pattern when one layer is twisted by 26° with respect to the other, which creates the pattern corresponding well to the experimental image in Figure 8g. Further details of the formation of this moiré pattern are described in Figure S29, Supporting Information with FFT analysis, IFFT filtered images, and schematic illustrations. The moiré pattern shown in Figure 8j resembles the moiré pattern observed in the growth of WS₂ on Pt deposited heating chip (Figure 7i). The FFT and schematic illustration in Figure 8k,l supports the fact that the twist by 9° of the layers of WS₂ in bilayer configuration generates the moiré pattern shown in Figure 8j. A detailed explanation of this type of moiré pattern was discussed in earlier sections of Pt deposited growth of WS₂ and in Figure S24, Supporting Information. Figure S30, Supporting Information depicts the larger picture of this type of moiré pattern formed on Au deposited chip along with its FFT in the inset. Another type of moiré pattern with a twist between the layers by 18° is shown in Figure S31, Supporting Information along with FFT, IFFT filtered images, and schematic illustrations. This type of moiré pattern was observed in small areas compared to the other two types which were found in larger scales. Figure S32, Supporting Information depicts the large view of WS₂ structures on the Pt deposited SiN_x window of the heating chip.

The two different types of moiré patterns were observed during the growth of WS₂ on Au deposited heating chips. During in situ TEM heating, mobility of Au particles was observed at higher temperatures (>500 °C), and the growth of WS₂ layers forming moiré patterns was also observed at the same temperatures. Mobility of Au particles beneath the WS₂ layers at higher temperatures might have triggered the rotation of WS₂ layers and led to the formation of various types of moiré patterns depending on the twist angles. Thus, Au particles and their catalytic reactivity with a precursor provided solubility limited growth of WS₂ layers which limited the bilayer thickness. As Au was not found to form sulfides by reacting with the sulfur in the precursor, it also helped to grow pure and single-crystal domains of WS₂.^[31,32] In contrast to the Au substrate case, Pt particles were observed to display very little mobility during the growth of WS₂ layers at high temperatures and limited the formation of different types of moiré patterns of WS₂ layers on Pt deposited heating chip. It was also observed on the Au deposited chip that the Au particles mostly don't stick to the

edges of WS₂ structures, leaving WS₂ structures free from Au particles and Au-WS₂ hybrid structures.

In both the Pt and Au deposited chip growth, the metal films (with random shape and size metal islands) were deliberately not annealed before using them in the in situ TEM heating to avoid the formation of islands and nanoparticles of metals (Pt and Au) before the growth of WS₂. This has avoided multiple nucleation centers that likely would have resulted in the smaller and multi-crystalline domains of WS₂.^[77] As the growth of WS₂ depends on the morphology of metal substrate, it would be interesting to see how WS₂ grows on a surface-treated substrate such as annealed and polished substrate. It has been observed earlier that monolayer WS₂ film was grown on surface-treated Au foil.^[32] The ATT precursor formed more continuous and thin structures on metal (Pt and Au) substrates compared to the growth observed on the bare SiN_x membrane. This in turn changed the overall growth process of horizontal layers of WS₂ on metal substrates. The weak interaction between WS₂ and Au was reported earlier,^[31] which enables a more easy transfer of the WS₂ layer to the desired substrate to enable use in applications.

The WS₂ layers showed good stability at 800 °C, and increasing the temperature further led to the removal of S atoms from WS₂ to form metal tungsten (W) islands by breaking the 2D structure as shown with frames captured from Movies S6, S7, Supporting Information in Figure S33a,b, Supporting Information. It has been observed for other 2D materials that, at high temperatures and/or under the influence of the electron beam, chalcogen atoms tend to sublime leaving metal behind.^[59] This transformation was observed in the earlier part where WS₂ was grown on SiN_x membrane and heated above 800 °C (as shown in Figure S17, Supporting Information). FFTs taken from the areas before and after transformation confirm the appearance of bcc W for both cases. This is shown in Figure S33, Supporting Information with the help of false-colored IFFT filtered images (Figure S33c,f,h,k, Supporting Information) and FFTs (Figure S33d,g,i,l, Supporting Information) for the corresponding structures. The bright spots in the FFT in Figure S33d, Supporting Information marked with yellow, white, and blue circles correspond to W crystal with {111}, {110}, and {002} patterns viewed along [001] direction. In the FFT of the area marked with green square in Figure S33j, Supporting Information, bright spots indicated in yellow, blue, and white circles correspond to bcc W crystal with {112}, {002}, and {110} patterns viewed along [110] direction. The interplanar distance 0.23, 0.16, and 0.13 nm correspond to {112}, {002}, and {110} planes of W. Thus hexagonal crystal structure of WS₂ transformed into the bcc W after heating to 900 °C. FFTs in Figure S33g,l, Supporting Information depict the bilayer WS₂ forming the moiré pattern by twist of one of the layers by 26° on both Pt and Au deposited chip, respectively. An estimation of the number of layers in twisted layers or horizontal structures on Pt film is presented in Figure S34, Supporting Information.

2.7. Ex Situ Growth of WS₂ on Pt and Au Deposited Chips

Finally, using the vacuum oven we investigated the ex situ growth of WS₂ on Pt and Au deposited heating chips. To this

end, the Pt and Au deposited chips were drop cast with ATT and heated in the vacuum oven, maintaining the temperature at 350 °C for 10 min in the middle of the heating profile to promote the growth. These chips were then introduced into the TEM to investigate the as-grown WS₂ structures. As shown in Figure S35, Supporting Information, a large area of WS₂ horizontal layers grew on the Pt deposited chip. A detailed analysis of this growth shows that the bilayer WS₂ with a twist with 26° grows onto (111) surface of Pt. FFT and IFFT filtered images shown in Figure S35, Supporting Information reveal the fact that along with bilayer growth of WS₂ there is a crystalline background that corresponds to Pt (111) surface. To enhance this background in the picture, the bright spots in the FFT pattern were masked and an IFFT of the unmasked area was generated. This confirms that during the ex situ heating of ATT precursor on the Pt deposited chip, the Pt surface displays predominantly the (111) surface and that WS₂ horizontal layers are grown on this surface. The formation of the Pt (111) surface helped in this process to achieve self-limited surface catalytic growth of WS₂, limiting the 2D WS₂ to two-layer thickness (as can be seen from the FFT). Similar results were obtained on the Au deposited chip and these results are shown in Figure S36, Supporting Information. In this case, the Au surface evolved along with the growth of WS₂ layers. The IFFT filtered images blocking the marked area show a background that reflects the Au surface. Thus in both cases, WS₂ horizontal layers grew on modified surfaces of Pt and Au. Though the ex situ heating might have modified the metal (Pt/Au) surfaces, the growth of WS₂ was obtained similar to the growth obtained during the in situ TEM heating experiments.

3. Conclusion

In summary, we observed growth dynamics of 2D WS₂ structures on amorphous SiN_x and on metal (Pt and Au) substrates using in situ TEM heating of a single solid-state precursor. Two different growth types are observed microscopically; vertical growth of WS₂ layers at thick precursor areas and horizontal growth of WS₂ layers at thin precursor areas. Either vertical or horizontal growth can therefore be initiated by controlling the thickness of the drop cast precursor. Layer-by-layer growth, which is taking place during the vertical growth in thicker areas, leads to the formation of larger vertical clusters of WS₂ layers that can be self-limited in the length of the 2D layers and the number of layers in the stack. During the growth of horizontal layers in thin precursor areas, various mechanisms such as oriented attachment, Ostwald ripening, coalescence, and merging of nanograins, as well as edge reconstructions, eventually lead to the formation of large and well-defined nanosheets of WS₂. By depositing Pt and Au on heating chips the growth of WS₂ structures was strongly enhanced, with the horizontal layers growing to a maximum thickness of 2 to 3 layers through solubility limited surface-mediated growth. On metal substrates, mutually twisted WS₂ layers were found through the observation of the associated moiré patterns in bilayer or trilayer configurations. The twist of WS₂ layers can be controlled through substrate treatments by inspection of the moiré patterns. The ex situ experiments validated the results of

the in situ measurements, with observations of similar types of growth on bare SiN_x and on metal (Pt and Au) deposited substrates. Our study offers a fundamental understanding of the growth of 2D WS₂ structures on different substrates and can be employed to design and fabricate 2D WS₂ and associated 2D TMDs for various catalytic and electronic applications.

4. Experimental Section

In Situ Transmission Electron Microscopy: In situ TEM heating experiments were performed on DENSolutions heating holder and Wildfire S3 heating chip with electron transparent ≈30 nm thick SiN_x windows. Before the in situ TEM heating, the samples were prepared by dissolving high purity (NH₄)₂WS₄ (ATT) (Sigma Aldrich, 99.9%) in ethanol to form 1% and 5% solutions. These solutions were sonicated for 15 min, and drop casted onto the plasma cleaned heating chip and dried in air. 1% solution was used to get thin precursor while 5% solution was used for thick precursor regions on the heating chip. The heating chip was then introduced into the FEI Talos F200X TEM operated at 200 kV for imaging. In all the TEM heating experiments, samples were preheated to 100 °C for at least 10 min to remove organic residues. The temperature was then increased from 100 to 900 °C in steps of 25 °C. During in situ TEM heating, after each 100 °C the temperature was held constant to observe and image growth changes in the first pilot experiment. Each TEM heating experiment was repeated at least five times. Scanning TEM (STEM) imaging on the FEI Talos F200X was conducted using a probe current of 30 pA and a dwell time per pixel of 4.0 μs. All EDS chemical mapping experiments were performed on the Talos F200X TEM equipped with a Chemi-STEM elemental analysis setup. Each of the EDS maps was recorded for 15 min to improve the signal-to-noise ratio. All of the EDS maps in the Supporting Information are presented in atomic percent. For all the filtered images in the Supporting Information, the contrast was improved between the material and the amorphous region in the background by applying a mask on the amorphous region followed by the IFFT for better display purposes. The images in Figures 3g,h,7e–h were applied with the GEM LUT effect in ImageJ software for better visualization. The TEM imaging simulation in Figure 3h was performed using QSTEM software. The simulated image was generated with the following settings: accelerating voltage: 200 kV, objective aperture: 15 mrad, convergence angle: 1 mrad, focal spread: 2 nm, defocus: 10.

Metal (Pt and Au) Film Deposition: The metal films (Pt and Au) with ≈5 nm thickness were deposited onto the heating chips using sputter coater equipment. A specific target was chosen to deposit the desired metal and settings were optimized to achieve ≈5 nm thickness of deposited material.

Ex Situ Experiments and Characterization: The ex situ heating experiments were performed in a vacuum oven Nabertherm RHTH tube oven with maximum of 1800 °C heating capacity at 2 mbar pressure. All the ex situ experiments reported in this article were performed at 350 °C for 10 min, after carrying a few pilot experiments at 350, 500, and 700 °C to optimize the growth temperature. The samples for ex situ vacuum oven growth were prepared similarly as they were made for in situ TEM heating. Except that, few samples were prepared in powder form to use them to characterize using Raman spectroscopy. Raman spectroscopic measurements were performed on Renishaw Raman spectroscope equipped with RL532C50 and RL633 HeNe laser giving 532 and 633 nm light, respectively and had maximum power of ≈12.5 mW. The presented spectroscopic results were performed at 532 nm excitation laser. The samples for Raman measurements were prepared by placing ex situ prepared powder samples of WS₂ directly onto the glass slides.

Supporting Information

Supporting Information is available from the Wiley Online Library or from the author.

Acknowledgements

This project was financially supported by the European Research Council through an ERC Consolidator Grant NANO-INSITU (No. 683076). The authors thank Hans Meeldijk and Chris Schneijdenberg from Electron Microscopy Utrecht for help with TEM experimentation, and thank Dr. Xiaobin Xie and Harith Gurunaryanan of Utrecht University for Raman spectroscopic measurements. The authors thank B.Sc. student Jesse Bückmann and Prof. Alfons van Blaaderen for useful discussions on the project. The authors also thank Dr. Rafael Gregorio Mendes and Xiaodan Chen for proofreading the manuscript.

Conflict of Interest

The authors declare no conflict of interest.

Data Availability Statement

The data that supports the findings of this study are available in the paper itself and in the Supporting Information of this article.

Keywords

2D growth mechanisms, catalytic metal substrates, ex situ growth, in situ transmission electron microscopy, thermolysis, twisted bilayers, WS₂

Received: September 9, 2021

Revised: September 29, 2021

Published online: October 20, 2021

- [1] L. Britnell, R. Ribeiro, A. Eckmann, R. Jalil, B. Belle, A. Mishchenko, Y.-J. Kim, R. Gorbachev, T. Georgiou, S. Morozov, *Science* **2013**, *340*, 1311.
- [2] M. Chhowalla, H. S. Shin, G. Eda, L.-J. Li, K. P. Loh, H. Zhang, *Nat. Chem.* **2013**, *5*, 263.
- [3] T. Georgiou, R. Jalil, B. D. Belle, L. Britnell, R. V. Gorbachev, S. V. Morozov, Y.-J. Kim, A. Gholinia, S. J. Haigh, O. Makarovskiy, *Nat. Nanotechnol.* **2013**, *8*, 100.
- [4] D. Ovchinnikov, A. Allain, Y.-S. Huang, D. Dumcenco, A. Kis, *ACS Nano* **2014**, *8*, 8174.
- [5] Q. H. Wang, K. Kalantar-Zadeh, A. Kis, J. N. Coleman, M. S. Strano, *Nat. Nanotechnol.* **2012**, *7*, 699.
- [6] L. Yang, N. A. Sinitsyn, W. Chen, J. Yuan, J. Zhang, J. Lou, S. A. Crooker, *Nat. Phys.* **2015**, *11*, 830.
- [7] H. Zeng, G.-B. Liu, J. Dai, Y. Yan, B. Zhu, R. He, L. Xie, S. Xu, X. Chen, W. Yao, *Sci. Rep.* **2013**, *3*, 1608.
- [8] N. Huo, J. Kang, Z. Wei, S. S. Li, J. Li, S. H. Wei, *Adv. Funct. Mater.* **2014**, *24*, 7025.
- [9] N. Peimyo, J. Shang, C. Cong, X. Shen, X. Wu, E. K. Yeow, T. Yu, *ACS Nano* **2013**, *7*, 10985.
- [10] X. Liu, J. Hu, C. Yue, N. D. Fera, Y. Ling, Z. Mao, J. Wei, *ACS Nano* **2014**, *8*, 10396.
- [11] A. L. Elías, N. Perea-López, A. Castro-Beltrán, A. Berkdemir, R. Lv, S. Feng, A. D. Long, T. Hayashi, Y. A. Kim, M. Endo, *ACS Nano* **2013**, *7*, 5235.
- [12] Y.-H. Lee, L. Yu, H. Wang, W. Fang, X. Ling, Y. Shi, C.-T. Lin, J.-K. Huang, M.-T. Chang, C.-S. Chang, *Nano Lett.* **2013**, *13*, 1852.
- [13] Y. Zhang, Y. Zhang, Q. Ji, J. Ju, H. Yuan, J. Shi, T. Gao, D. Ma, M. Liu, Y. Chen, *ACS Nano* **2013**, *7*, 8963.
- [14] M. Chubarov, T. H. Choudhury, D. R. Hickey, S. Bachu, T. Zhang, A. Sebastian, A. Bansal, H. Zhu, N. Trainor, S. Das, *ACS Nano* **2021**, *15*, 2532.
- [15] A. Cohen, A. Patsha, P. K. Mohapatra, M. Kazes, K. Ranganathan, L. Houben, D. Oron, A. Ismach, *ACS Nano* **2020**, *15*, 526.
- [16] C. Cong, J. Shang, X. Wu, B. Cao, N. Peimyo, C. Qiu, L. Sun, T. Yu, *Adv. Opt. Mater.* **2014**, *2*, 131.
- [17] Y. Yue, J. Chen, Y. Zhang, S. Ding, F. Zhao, Y. Wang, D. Zhang, R. Li, H. Dong, W. Hu, *ACS Appl. Mater. Interfaces* **2018**, *10*, 22435.
- [18] Y. Jung, J. Shen, Y. Liu, J. M. Woods, Y. Sun, J. J. Cha, *Nano Lett.* **2014**, *14*, 6842.
- [19] W. Zhao, Z. Ghorannevis, L. Chu, M. Toh, C. Kloc, P.-H. Tan, G. Eda, *ACS Nano* **2013**, *7*, 791.
- [20] I. Datta, S. H. Chae, G. R. Bhatt, M. A. Tadayon, B. Li, Y. Yu, C. Park, J. Park, L. Cao, D. Basov, *Nat. Photonics* **2020**, *14*, 256.
- [21] X. Zhang, C. De-Eknankul, J. Gu, A. L. Boehmke, V. M. Menon, J. Khurgin, E. Cubukcu, *Nat. Nanotechnol.* **2019**, *14*, 844.
- [22] Y. Yang, H. Fei, G. Ruan, Y. Li, J. M. Tour, *Adv. Funct. Mater.* **2015**, *25*, 6199.
- [23] D. Voiry, H. Yamaguchi, J. Li, R. Silva, D. C. Alves, T. Fujita, M. Chen, T. Asefa, V. B. Shenoy, G. Eda, *Nat. Mater.* **2013**, *12*, 850.
- [24] T. Prasad, E. Diemann, A. Müller, *J. Inorg. Nucl. Chem.* **1973**, *35*, 1895.
- [25] J. Espino, L. Alvarez, C. Ornelas, J. Rico, S. Fuentes, G. Berhault, G. Alonso, *Catal. Lett.* **2003**, *90*, 71.
- [26] O. A. Abbas, I. Zeimpekis, H. Wang, A. H. Lewis, N. P. Sessions, M. Ebert, N. Aspiotis, C.-C. Huang, D. Hewak, S. Mailis, *Sci. Rep.* **2020**, *10*, 1696.
- [27] M. A. Worsley, S. J. Shin, M. D. Merrill, J. Lenhardt, A. J. Nelson, L. Y. Woo, A. E. Gash, T. F. Baumann, C. A. Orme, *ACS Nano* **2015**, *9*, 4698.
- [28] J. Chen, G. H. Ryu, Q. Zhang, Y. Wen, K.-L. Tai, Y. Lu, J. H. Warner, *ACS Nano* **2019**, *13*, 14486.
- [29] P. Liu, T. Luo, J. Xing, H. Xu, H. Hao, H. Liu, J. Dong, *Nanoscale Res. Lett.* **2017**, *12*, 1.
- [30] H. R. Gutiérrez, N. Perea-López, A. L. Elías, A. Berkdemir, B. Wang, R. Lv, F. López-Urías, V. H. Crespi, H. Terrones, M. Terrones, *Nano Lett.* **2013**, *13*, 3447.
- [31] Y. Gao, Z. Liu, D.-M. Sun, L. Huang, L.-P. Ma, L.-C. Yin, T. Ma, Z. Zhang, X.-L. Ma, L.-M. Peng, H.-M. Cheng, W. Ren, *Nat. Commun.* **2015**, *6*, 8569.
- [32] S. J. Yun, S. H. Chae, H. Kim, J. C. Park, J.-H. Park, G. H. Han, J. S. Lee, S. M. Kim, H. M. Oh, J. Seok, *ACS Nano* **2015**, *9*, 5510.
- [33] T.-Y. Lin, Y.-L. Chen, C.-F. Chang, G.-M. Huang, C.-W. Huang, C.-Y. Hsieh, Y.-C. Lo, K.-C. Lu, W.-W. Wu, L.-J. Chen, *Nano Lett.* **2018**, *18*, 778.
- [34] C. B. Maliakkal, D. Jacobsson, M. Tornberg, A. R. Persson, J. Johansson, R. Wallenberg, K. A. Dick, *Nat. Commun.* **2019**, *10*, 4577.
- [35] Q. Sun, D. Pan, M. Li, J. Zhao, P. Chen, W. Lu, J. Zou, *Nanoscale* **2020**, *12*, 11711.
- [36] Z. Zhang, N. Liu, L. Li, J. Su, P.-P. Chen, W. Lu, Y. Gao, J. Zou, *Nano Lett.* **2018**, *18*, 6597.
- [37] I. Cora, Z. Fogarassy, R. Fornari, M. Bosi, A. Rečnik, B. Pécz, *Acta Mater.* **2020**, *183*, 216.
- [38] J. Cui, H. Zheng, K. He, *Adv. Mater.* **2021**, *33*, 2000699.
- [39] M. Singh, C. Ghosh, P. Kotula, J. Watt, H. Silva, C. B. Carter, *Microsc. Microanal.* **2020**, *26*, 1418.
- [40] M. A. van Huis, N. P. Young, G. Pandraud, J. F. Creemer, D. Vanmaekelbergh, A. I. Kirkland, H. W. Zandbergen, *Adv. Mater.* **2009**, *21*, 4992.
- [41] K. Berlin, A. Trampert, *J. Phys. Chem.* **2018**, *122*, 2968.
- [42] J. Buha, R. Gaspari, A. E. Del Rio Castillo, F. Bonaccorso, L. Manna, *Nano Lett.* **2016**, *16*, 4217.
- [43] F. Cheng, L. Lian, L. Li, J. Rao, C. Li, T. Qi, Y. Cheng, Z. Zhang, J. Zhang, J. Wang, *Nano Energy* **2020**, *75*, 104816.

- [44] D. J. Hellebusch, K. Manthiram, B. J. Beberwyck, A. P. Alivisatos, *J. Phys. Chem. Lett.* **2015**, *6*, 605.
- [45] J. Li, Z. Wang, Y. Li, F. L. Deepak, *Adv. Sci.* **2019**, *6*, 1802131.
- [46] C. Luo, J. Li, X. Yang, X. Wu, S. Zhong, C. Wang, L. Sun, *ACS Appl. Nano Mater.* **2020**, *3*, 4747.
- [47] Q. Yu, M.-M. Mao, Q.-J. Li, X.-Q. Fu, H. Tian, J.-X. Li, S. X. Mao, Z. Zhang, *Nano Lett.* **2016**, *16*, 1156.
- [48] Z. Dang, J. Shamsi, F. Palazon, M. Imran, Q. A. Akkerman, S. Park, G. Bertoni, M. Prato, R. Brescia, L. Manna, *ACS Nano* **2017**, *11*, 2124.
- [49] M. Gocyla, S. Kuehl, M. Shviro, H. Heyen, S. Selve, R. E. Dunin-Borkowski, M. Heggen, P. Strasser, *ACS Nano* **2018**, *12*, 5306.
- [50] Y. Yuan, K. Amine, J. Lu, R. Shahbazian-Yassar, *Nat. Commun.* **2017**, *8*, 15806.
- [51] R. G. Mendes, J. Pang, A. Bachmatiuk, H. Q. Ta, L. Zhao, T. Gemming, L. Fu, Z. Liu, M. H. Rummeli, *ACS Nano* **2019**, *13*, 978.
- [52] G. H. Ryu, A. France-Lanord, Y. Wen, S. Zhou, J. C. Grossman, J. H. Warner, *ACS Nano* **2018**, *12*, 11638.
- [53] X. Sang, X. Li, W. Zhao, J. Dong, C. M. Rouleau, D. B. Geohegan, F. Ding, K. Xiao, R. R. Unocic, *Nat. Commun.* **2018**, *9*, 2051.
- [54] K. L. Tai, C. W. Huang, R. F. Cai, G. M. Huang, Y. T. Tseng, J. Chen, W. W. Wu, *Small* **2020**, *16*, 1905516.
- [55] Y.-T. Tseng, K.-L. Tai, C.-W. Huang, C.-Y. Huang, W.-W. Wu, *J. Phys. Chem.* **2020**, *124*, 14935.
- [56] D. S. Gavhane, H. van Gog, B. Thombare, G. Lole, L. C. Post, M. A. More, M. A. van Huis, *npj 2D Mater. Appl.* **2021**, *5*, 24.
- [57] J. Chen, G. H. Ryu, S. Sinha, J. H. Warner, *ACS Nano* **2019**, *13*, 8256.
- [58] G. H. Ryu, J. Chen, Y. Wen, J. H. Warner, *Chem. Mater.* **2019**, *31*, 9895.
- [59] E. Sutter, Y. Huang, H.-P. Komsa, M. Ghorbani-Asl, A. Krashennikov, P. Sutter, *Nano Lett.* **2016**, *16*, 4410.
- [60] X. Li, M. Sun, C. Shan, Q. Chen, X. Wei, *Adv. Mater. Interfaces* **2018**, *5*, 1701246.
- [61] L. Fei, S. Lei, W.-B. Zhang, W. Lu, Z. Lin, C. H. Lam, Y. Chai, Y. Wang, *Nat. Commun.* **2016**, *7*, 12206.
- [62] X. Sang, X. Li, A. A. Puzos, D. B. Geohegan, K. Xiao, R. R. Unocic, *Adv. Funct. Mater.* **2019**, *29*, 1902149.
- [63] N. Kondekar, M. G. Boebinger, M. Tian, M. H. Kirmani, M. T. McDowell, *ACS Nano* **2019**, *13*, 7117.
- [64] B. C. Bayer, R. Kaindl, M. Reza Ahmadpour Monazam, T. Susi, J. Kotakoski, T. Gupta, D. Eder, W. Waldhauser, J. C. Meyer, *ACS Nano* **2018**, *12*, 8758.
- [65] Y. Zhang, Z. Zhang, Y. Cheng, F. Cheng, L. Wang, N. Liu, L. Li, J. Su, Y. Gao, *Nano Energy* **2020**, *67*, 104221.
- [66] D. Hunyadi, A. L. V. M. Ramos, I. M. Szilágyi, *J. Therm. Anal. Calorim.* **2015**, *120*, 209.
- [67] F. Börrnert, S. M. Avdoshenko, A. Bachmatiuk, I. Ibrahim, B. Büchner, G. Cuniberti, M. H. Rummeli, *Adv. Mater.* **2012**, *24*, 5630.
- [68] C. Stern, S. Grinvald, M. Kirshner, O. Sinai, M. Oksman, H. Alon, O. E. Meiron, M. Bar-Sadan, L. Houben, D. Naveh, *Sci. Rep.* **2018**, *8*, 16480.
- [69] D. Ugarte, *Nature* **1992**, *359*, 707.
- [70] W. Zheng, X. Zhao, W. Fu, *ACS Appl. Mater. Interfaces* **2021**, *13*, 9561.
- [71] M. A. Van Huis, L. T. Kunneman, K. Overgaag, Q. Xu, G. Pandraud, H. W. Zandbergen, D. Vanmaekelbergh, *Nano Lett.* **2008**, *8*, 3959.
- [72] C. Schliehe, B. H. Juárez, M. Pelletier, S. Jander, D. Greshnykh, M. Nagel, A. Meyer, S. Foerster, A. Kornowski, C. Klinke, *Science* **2010**, *329*, 550.
- [73] C. Van Overbeek, J. L. Peters, S. A. Van Rossum, M. Smits, M. A. Van Huis, D. Vanmaekelbergh, *J. Phys. Chem.* **2018**, *122*, 12464.
- [74] M. Seol, M. H. Lee, H. Kim, K. W. Shin, Y. Cho, I. Jeon, M. Jeong, H. I. Lee, J. Park, H. J. Shin, *Adv. Mater.* **2020**, *32*, 2003542.
- [75] N. Salazar, S. Rangarajan, J. Rodríguez-Fernández, M. Mavrikakis, J. V. Lauritsen, *Nat. Commun.* **2020**, *11*, 4369.
- [76] A. Azizi, X. Zou, P. Ercius, Z. Zhang, A. L. Elías, N. Perea-López, G. Stone, M. Terrones, B. I. Yakobson, N. Alem, *Nat. Commun.* **2014**, *5*, 4867.
- [77] A. Patsha, V. Sheff, A. Ismach, *Nanoscale* **2019**, *11*, 22493.